Tracing elevated abundance of CH_2Cl_2 in the subarctic upper troposphere to the Asian Summer Monsoon

Markus Jesswein[1], Valentin Lauther[2], Nicolas Emig[3], Peter Hoor[3], Timo Keber[1], Hans-Christoph Lachnitt[3], Linda Ort[4], Tanja Schuck[1], Johannes Strobel[2], Ronja Van Luijt[2], C. Michael Volk[2], Franziska Weyland[3], and Andreas Engel[1]

[1]University of Frankfurt, Institute for Atmospheric and Environmental Sciences, Frankfurt, Germany
[2]Institute for Atmospheric and Environmental Research, University of Wuppertal, Wuppertal, Germany
[3]Johannes Gutenberg University of Mainz, Institute for Atmospheric Physics, Mainz, Germany
[4]Atmospheric Chemistry Department, Max Planck Institute for Chemistry, Mainz, Germany

Correspondence: Markus Jesswein (jesswein@iau.uni-frankfurt.de)

Abstract.

The Asian Summer Monsoon (ASM) is a seasonal weather pattern characterized by heavy rains and winds, mainly affecting South and Southeast Asia during the summer months. The deep convection within the ASM is an important transport process for pollutants from the planetary boundary layer up to the tropopause region. This study uses in situ observations of CH_2Cl_2 from the PHILEAS aircraft campaign in late summer 2023 to examine the transport pathways and timescales for polluted air from the ASM to the extratropical upper troposphere and lower stratosphere (UTLS). CH_2Cl_2 mixing ratios of up to 300 ppt ($\approx 500\%$ of the northern hemisphere background) were measured in the upper troposphere in the subarctic region. The three largest observed pollution events were analyzed with the help of the Lagrangian particle dispersion model FLEXPART, both in terms of their origin and their potential entry into the lower stratosphere. The results show that the East Asian Summer Monsoon (EASM) is the key pathway for transporting uncontrolled Cl-VSLS into the tropopause region, which contributes to an increase in tropospheric background levels with the potential to enter the lower stratosphere. The transport analysis of elevated mixing ratios shown here suggests that transport to the upper troposphere in the subarctic region did not occur through transport into the Asian Summer Monsoon Anticyclone (ASMA) with subsequent eddy-shedding events, but rather by large convective transport contributions from the EASM. The projected entry into the lower stratosphere in the following days amounts to a few percent, indicating that the direct influence of these particular events on the lower stratosphere is probably minor.

1 Introduction

Short-lived chlorinated substances (Cl-VSLS) have shown increasing abundance in the atmosphere in recent years. These trace gases have local lifetimes less than half a year and are not controlled by the Montreal Protocol or its amendments and adjustments. The trace gases themselves and their product gases can reach the stratosphere and participate in catalytic cycles that destroy ozone with a general contribution depending on the spatial and temporal variability of their sources, transport

pathways and chemical transformation (Laube and Tegtmeier, 2022). Model simulations conducted by Bednarz et al. (2023) indicate that Cl-VSLS caused a decrease of approximately 2–3 DU (Dobson units) in the springtime at high latitudes during the second decade of the 21st century. Therefore, a continued increase in Cl-VSLS concentrations may postpone future recovery
25 of the ozone layer (Hossaini et al., 2017).

Dichloromethane (CH_2Cl_2) is the most abundant Cl-VSLS in the atmosphere with mainly anthropogenic sources that make up around 90% of global emissions and a minor contribution from natural sources (Montzka et al., 2010; Laube and Tegtmeier, 2022). The atmospheric lifetime is estimated to be around 176 days (95–1070 days) (Burkholder et al., 2022). Between 2000 and 2020, global emissions increased by a factor of 2.5 to approximately 1.1 to 1.3 Tg yr^{-1} (Laube and Tegtmeier, 2022).
30 Regional increases in emissions from the Asian region are the substantial part of the global increase (e.g. Claxton et al., 2020; An et al., 2021). In 2020, the global mean abundance of CH_2Cl_2 was around 40–45 ppt and thus nearly twice the amount compared to the early part of the century (Laube and Tegtmeier, 2022).

The Asian Summer Monsoon (ASM) is a seasonal weather pattern characterized by heavy rains and winds, mainly affecting South and Southeast Asia during the summer months. Within the ASM region, deep convection rapidly transports air from the
35 planetary boundary layer (PBL) to the upper troposphere and lower stratosphere (UTLS) (e.g. Pan et al., 2016). Furthermore, the ASM forms a high pressure system in the UTLS, the Asian Summer Monsoon Anticyclone (ASMA), which confines uplifted pollutants (e.g. Park et al., 2007; Ploeger et al., 2015). However, the isolation of the ASMA is not perfect and there is, to some extent, horizontal exchange between ASMA and its surrounding by wave breaking or the so-called eddy shedding (e.g. Garny and Randel, 2016; Clemens et al., 2022).
40 The ASM itself consists of three subcomponents: the South Asian Summer Monsoon (SASM), the East Asian Summer Monsoon (EASM), and the Western North Pacific Summer Monsoon (WNPSM) (e.g. Ha et al., 2017). The latter constitutes an oceanic monsoon system. Thus, SASM and EASM are the two systems that influence continental areas with potentially polluted regions. The differential heating between the Indian and Pacific oceans and continental land masses governs SASM and EASM, with the Monsoon Trough serving as the main convergence zone in the SASM area and the East Asia subtropical
45 front in the EASM region (Pan et al., 2022, 2024). Li et al. (2022) examined the outputs from CMIP6 models to reveal the physical processes driving the unique changes in circulation in SASM and EASM due to global warming. Their findings consistently indicate a projected strengthening of the EASM circulation and a weakening of the SASM circulation in a future warmer climate.

Only a handful of airborne observations show the influence of ASM transport into the UTLS with respect to Cl-VSLS (e.g.
50 Oram et al., 2017; Adcock et al., 2021; Treadaway et al., 2022; Lauther et al., 2022; Pan et al., 2024). The most recent work by Pan et al. (2024) highlights EASM convection as an effective transport pathway for Cl-VSLS. They found extremely high values of CH_2Cl_2 (up to 600 ppt) in the region near the tropopause of East Asia during the ACCLIP (Asian Summer Monsoon Chemical and Climate Impact Project) campaign in August 2022. These substantial abundances arise due to the active deep EASM convection and the convergence zone directly over the primary Cl-VSLS emission sources (Pan et al., 2024).
55 This study uses in situ observations of CH_2Cl_2 from the PHILEAS (Probing High Latitude Export of Air from the Asian Summer Monsoon) aircraft campaign in 2023 to examine the transport pathways and timescales of CH_2Cl_2 from the ASM to

the extratropical UTLS with the support of the Lagrangian particle dispersion model FLEXPART. Sect. 2 outlines the in situ measurements, the application of FLEXPART, and the analysis of synoptic situations. In Sect. 3, we compare the observations of two in situ instruments. Furthermore, an analysis of the three events that show the highest CH_2Cl_2 mixing ratios in the upper troposphere during the PHILEAS campaign is carried out, focusing on their origins and potential for further transport into the stratosphere. We briefly discuss our results in Sect. 4 and end with a summary and conclusion in Sect. 5.

2   Methods

2.1   The PHILEAS campaign 2023

The recent High Altitude and Long Range Research Aircraft (HALO) campaign PHILEAS, undertaken in August and September 2023, had as one of its objectives the investigation of the primary transport pathways and time scales for polluted air from the Asian Summer Monsoon (ASM) into the extratropical upper troposphere and lower stratosphere (UTLS) (Riese et al., 2025, submitted). Throughout the PHILEAS campaign, a total of 20 flights were conducted, comprising 18 flights dedicated to scientific research and two flights aimed at calibrating turbulence measurements and assessing the electromagnetic compatibility between the instruments and the aircraft. The first phase took place in Oberpfaffenhofen, Germany, to investigate rather undiluted air from the ASMA and background lowermost stratospheric air. The second major phase was conducted from Anchorage, Alaska, tracing polluted air masses uplifted in the ASM and transported across the Pacific to the high-latitude UTLS. A final background flight was performed from Oberpfaffenhofen, with the two transfer flights between the two locations also serving as research flights. The flights encompass a potential temperature (Θ) range from 277 to 408 K (altitude range from ground to approximately 15 km). A more detailed description of all flights of the PHILEAS campaign is provided in the Table S 1 in the supporting information (SI). Furthermore, the flight tracks of the scientific flights are shown in Figures S 1 to S 3 in the SI.

2.2   in situ trace gas measurements

The HALO aircraft was equipped with a wide range of different in situ and remote sensing instruments (Riese et al., 2025, submitted). For the analysis, only in situ observations of three instruments are used, which are described in the following sections. In addition to the scientific instruments, temporarily installed for the campaign, the Basic HALO Measurements and Sensor System (BAHAMAS) is part of HALO. This permanently installed instrument provides meteorological and aircraft parameters along the flight tracks (Krautstrunk and Giez, 2012).

2.2.1 CH_2Cl_2 observations

Dichloromethane (CH_2Cl_2) mixing ratios were measured using two distinct instruments on board the HALO research aircraft, the GhOST (Gas chromatograph for Observational Studies using Tracers) instrument from the University of Frankfurt and the HAGAR-V (High Altitude Gas AnalyzeR - five-channel version) instrument from the University of Wuppertal. Details on

the characteristics of these two instruments are provided in previous publications, including Jesswein et al. (2021) and Keber et al. (2020) for the GhOST instrument and Lauther et al. (2022) for a previous configuration of the HAGAR-V instrument. CH_2Cl_2 is measured with both instruments using gas chromatography (GC) and mass spectrometry (MS) with cryogenic sample preconcentration.

The GhOST includes a single GC-MS channel, sampling ambient air for 147 seconds with subsequent analysis, which leads to a time resolution of around 6 min per measurement cycle. Regular calibration measurements were performed during the research flights, and the measurement precision was derived for each flight from the standard deviation of these measurements. The average precision of CH_2Cl_2 throughout the PHILEAS campaign was 0.9%.

The HAGAR-V includes a two-channel GC with one MS. Using two GC systems can enhance the range of observable atmospheric trace gases or, by targeting the same species on both channels, doubles the frequency of observations (Lauther et al., 2022). The latter setup was selected during the PHILEAS campaign. With an ambient air sampling time of 30 seconds, a time resolution with the combined channels of 2 min is achieved. Similar to the GhOST, HAGAR-V is calibrated in-flight, but with two calibration gases. The average precision of CH_2Cl_2 throughout the PHILEAS campaign was 1.3%.

The calibration main gas bottles of both instruments, as well as the in-flight calibration gas cylinders, which were filled from the main gas bottles, were calibrated at the University of Frankfurt using a laboratory GC/MS (Schuck et al., 2018) or a Medusa (e.g. Miller et al., 2008; Arnold et al., 2012) system. The calibration relies on AGAGE-derived calibration according to the SIO-14 scale for CH_2Cl_2. All scientific flights were included in the analysis, except flight F02 due to malfunctions with the GhOST instrument for this flight.

2.2.2 N_2O observations

N_2O measurements were performed with the University of Mainz Airborne Quantum Cascade Laser Spectrometer (UMAQS). The instrument is based on direct absorption spectroscopy using a continuous-wave quantum cascade laser with a sweep rate of 2 kHz (Müller et al., 2015). The instrument consists of two units, each of which is equipped with a multipath cell (Herriott cell) with a path length of 76 m, operated at 40 Torr during PHILEAS. The instrument is calibrated in situ with two different working standards of compressed ambient air, which are compared to NOAA standards before and after the mission. Total uncertainty for N_2O is 0.08 ppb. The overall uncertainty can be obtained by adding the uncertainty for the working standards traceable to NOAA, which is 0.13 ppb for N_2O.

2.3 FLEXPART trajectories

Trajectory simulations were performed using version 11 of the Lagrangian particle dispersion model FLEXPART (Bakels et al., 2024). This is the newest version of the model, which was developed more than two decades ago (Stohl et al., 1998) with several improvements in between (e.g., Stohl et al., 2005; Pisso et al., 2019). Since then, this model has found application in numerous studies on atmospheric transport.

Central for our study is the effect of transport from the PBL and convection, including turbulence and subgrid winds. Therefore, we use FLEXPART, which utilizes motion vectors. These motion vectors combine the grid-scale wind velocity from

120   linearly interpolated meteorological input data and the parameterized turbulent velocity. In addition, particles may be vertically displaced by convection (Bakels et al., 2024). FLEXPART accounts for subgrid-scale convection using the parameterization scheme of Emanuel and Živković Rothman (1999), which relies on the grid-scale temperature and humidity fields and calculates the convective displacement of the particles (Stohl et al., 2005). FLEXPART differentiates turbulence in the atmospheric boundary layer (ABL) and turbulence in the free troposphere and stratosphere. Inside the ABL, turbulence is based on Hanna

125   (1982) and Ryall and Maryon (1998), and a skewed turbulence option by Cassiani et al. (2015) (more information can be found in Bakels et al. (2024)). Above the ABL, turbulent velocities are computed following Legras et al. (2003). A constant vertical diffusivity is used in the stratosphere, whereas a horizontal diffusivity is used in the free troposphere. These diffusivities (D_i) are converted into velocity scales using $\sigma_{vi} = \sqrt{2D_i/\Delta t}$, where i is the direction (Bakels et al., 2024).

    The model is driven by the most recent ERA5 (Hersbach et al., 2020) hourly reanalysis data of the ECMWF (European

130   Center for Medium-Range Forecasts), on a horizontal resolution of 0.5°x 0.5°. An important improvement of FLEXPART version 11 is the usage of the native vertical coordinates of ECMWF instead of interpolation to terrain-adapted coordinates with an improvement in trajectory accuracy and the better option for input and output of particle properties (Bakels et al., 2024).

    The particles are released in rectangular boxes bounded by the longitude, latitude, and pressure sampled by the aircraft in

135   the respective 5-minute intervals. Within each box, 5000 computational particles are released which are distributed evenly throughout the box. The trajectories of the particles are calculated for 12 days (forward and backward in time). Loss processes due to deposition or chemical reactions are neglected, with transport being the focus only. The information related to each particle is written as an hourly output, containing its position and meteorological information such as temperature, pressure, the height of the ABL, and potential vorticity, to name the most important ones for this study.

140 **2.4 ERA5 reanalysis - climatologic and synoptic situation**

We used ERA5 hourly data on single level and pressure levels (Copernicus Climate Change Service, 2018) to assess the climatological situation of the Asian Summer Monsoon (ASM) and the synoptic meteorological situation at the time of the PHILEAS campaign. The focus is on the Northern Hemisphere from 0 to 180°E and pressure levels range from 850 hPa to up to 150 hPa with a horizontal resolution of 0.25°x 0.25°for the months of August and September 2023. Parameters such as

145   convective available potential energy (CAPE) and total cloud cover were used. We derived several parameters from the ERA5 variables for the analysis of the meteorological situation.

    The equivalent thickness is the vertical distance between two pressure levels. The thickness is related to the density and temperature of the air, with decreasing thickness for colder air and increasing thickness for warmer air. Zones of high-thickness gradients help to identify fronts and boundaries between air masses.

150   Another parameter for frontal analysis is the Thermal Front Parameter (TFP) (Renard and Clarke, 1965; Hewson, 1998). The TFP describes the spatial change in the absolute value of the temperature gradient, but only the part of it that points in the direction of the temperature gradient. The mathematical definition is

$$TFP = \nabla|\nabla T| * \frac{\nabla T}{|\nabla T|} \tag{1}$$

with T the temperature or the equivalent potential temperature and defining a threshold value to be exceeded to define a front, e.g. a TFP > 1 K $(100\,\text{km})^{-2}$ (e.g. Kitabatake, 2008). The maximum of the TFP is located on the warm side of the zones with high thickness gradients. Thus, a combination of both parameters is well suited for the interpretation of front analyses. In the following, we use an equivalent thickness of 850 to 500 hPa, together with the TFP at 700 hPa.

The Q-Vector is an atmospheric dynamic parameter well suited for analyzing vertical motion in synoptic-scale weather systems, first introduced by Hoskins et al. (1978). It is the rate of change of the horizontal temperature gradient, following the geostrophic flow. Included are changes in both magnitude and orientation. The Q-Vector is defined in Bluestein (1992) as follows

$$\boldsymbol{Q} = -\frac{R_d T}{\sigma}\left(\frac{\partial \boldsymbol{v_g}}{\partial x}\nabla T, \frac{\partial \boldsymbol{v_g}}{\partial y}\nabla T\right) \tag{2}$$

with R_d the specific gas constant for dry air, σ the static stability, and $\boldsymbol{v_g}$ the geostrophic wind. The Q-Vector form of the omega equation (Eq. 3) can be helpful in finding areas of uplift and subsidence on a synoptic scale.

$$\left(\nabla^2 + \frac{f_0^2}{\sigma}\frac{\partial^2}{\partial p^2}\right)\omega = -2\nabla\boldsymbol{Q} \tag{3}$$

f_0 in the equation is a constant Coriolis parameter. Thus, $-2\nabla\boldsymbol{Q}$ determines the forcing for vertical motions with $2\nabla\boldsymbol{Q} > 0$ ($2\nabla\boldsymbol{Q} < 0$) associated with sinking (rising) motion (e.g. Lackmann, 2011). This study presents the Q-Vector and its divergence at the 500 hPa level.

3 Results

3.1 Asian Summer Monsoon in 2023

In 2023, the Asian Summer Monsoon occurred under El Niño conditions after three consecutive years of La Niña. However, El Niño conditions did not fully manifest in the atmosphere and ocean until early September. The rainfall in the ASM region showed typical levels, but exhibited significant spatial and temporal variability. South Korea experienced higher than average precipitation. In China, the precipitation in June was below average, while it was above average in August and September (World Meteorological Organization, 2024). Riese et al. (2025) (submitted) employed the CLaMS model and multiple origin tracers, collectively referred to as a South Asia tracer, to place PHILEAS measurements within a climatological context, focusing on transport from the Asian Summer Monsoon. They show that in 2023, there was a slight northward displacement of the eastward outflow accompanied by a somewhat more intense than average flushing of the lowermost stratosphere.

3.2 Major events of elevated CH$_2$Cl$_2$ in the upper troposphere

Dichloromethane mixing ratios were measured by two in situ instruments during the PHILEAS campaign. Figure S 4 in the SI presents the observations from both instruments as a function of potential temperature. When comparing the measurements, the HAGAR-V instrument's higher time resolution captured multiple observations within a single measurement period of the GhOST instrument. Averaging HAGAR-V observations over the time periods corresponding to the enrichment of the GhOST sample, as shown in Figure 1, reveals that the CH$_2$Cl$_2$ measurements from both instruments exhibit a slope of nearly 1 to 1, indicating excellent agreement, as confirmed by orthogonal distance regression (slope of 1.0074). We thus use observations of both instruments in the following.

Using the relationship of CH$_2$Cl$_2$ and N$_2$O (Fig. 2 A), periods with considerably increased CH$_2$Cl$_2$ without similarly increasing N$_2$O can be identified. N$_2$O, a long-lived greenhouse gas, has an atmospheric lifetime of approximately 116±9 years (Prather et al., 2015). It is well mixed throughout the troposphere, and its primary removal mechanism is through photochemical destruction processes in the stratosphere. Furthermore, Figure 2 A shows the median polynomial fit and the 90th and 10th percentile polynomial fit (all polynomials of degree 3), within which 80% of the observations are located. For mixing ratios below approximately 330 ppb N$_2$O, a rather compact relationship is observed between N$_2$O and CH$_2$Cl$_2$. Only during flight F07, several elevated mixing ratios were detected by both instruments. For N$_2$O mixing ratios that are approximately above 330 ppb, a clear partitioning of very high and less pronounced lower values of CH$_2$Cl$_2$ can be recognized.

We used the median fit function of the CH$_2$Cl$_2$-N$_2$O relationship to identify the major elevated observations during PHILEAS. For each CH$_2$Cl$_2$ observation, we derived a corresponding median CH$_2$Cl$_2$ mixing ratio (CH$_2$Cl$_{2med}$) using the respective N$_2$O mixing ratio and the median fit function. To more effectively highlight observations that substantially diverge from the median, the deviation (ΔCH$_2$Cl$_2$) is determined by subtracting CH$_2$Cl$_{2med}$ from the observed CH$_2$Cl$_2$ value for each observation. ΔCH$_2$Cl$_2$ is displayed as letter-value plots for every flight in Figure 2 B. The plots originate from a central line representing the median. Moving outwards, each subsequent letter-layer encompasses half of the residual data, beginning with the 50th percentile that includes 50 % of the data. Following this, the subsequent two segments hold 25 % of the data, continuing this pattern until only outliers are evident. Letter-value plots provide more detailed information in the tails compared to box plots, but only where the letter values reliably represent the corresponding quantiles (Hofmann et al., 2011). Four flights stand out where CH$_2$Cl$_2$ mixing ratios considerably higher than 100 ppt above CH$_2$Cl$_{2med}$ were observed. These are the flights F08, F09, F16, and F17. Three more flights show ΔCH$_2$Cl$_2$ between 50 and 100 ppt.

To determine the periods in which extremely high levels (elevated events) of CH$_2$Cl$_2$ were observed during the flights, we only consider observations that are above the mixing ratio derived from the fit of the 90th percentile curve and a factor of 2 above the median. In addition, an elevated event must have a duration of at least 10 minutes without any observation situated between elevated observations that is not itself considered elevated.

The CH$_2$Cl$_2$ time series of F08 and F17 are shown in Figure 3 A and Figure 4 A with elevated events shaded in red. This work focuses on these two flights. The CH$_2$Cl$_2$ time series with elevated events shaded from all four flights (F08, F09, F16, and F17) can be found in the supporting information (Figure S 5). The events in F09 show less coherent structures compared to those of

the other three flights. F08 shows a similar high CH_2Cl_2 deviation to F16, but its letter-plot tailing towards larger deviations is slightly more pronounced (see Fig. 2 B). F17 shows the most pronounced deviation from the median and the overall largest

215 mixing ratios of CH_2Cl_2 measured during the PHILEAS campaign. These two flights show three very clear events with CH_2Cl_2 mixing ratios of 200 to 300 ppt at an altitude of about 11 to 12.5 km and 330 to 350 K potential temperature (Θ) across the northwestern Pacific to the subarctic region of Alaska (Fig. 3 B and 4 B). In the upper troposphere at comparable potential temperatures, PHILEAS observations within the 10th and 90th percentile ranged from 50 ppt to 80 ppt. Figure 5 displays the flight tracks of these two flights with highlighted segments of the three elevated events.

3.3 The origin of elevated CH_2Cl_2 events

To further investigate the origins of the observed elevated CH_2Cl_2 mixing ratios, we utilize the Lagrangian particle dispersion model FLEXPART, running it in backward mode to trace the origins of air masses. Computational air particles, released on the flight path, were followed backward in time until they reached the PBL. Figures 3 C and 4 C display the median latitude and longitude (only 0–180°E to simplify presentation) of last PBL contacts of released particles within 5 min intervals along the

225 flight tracks. The backward trajectories indicate a large variability in the median PBL contacts, and the CH_2Cl_2 mixing ratios appear to be sensitive to the last PBL identified by the simulations. This suggests that air masses collected along the flight paths were influenced by various transport histories and were impacted by different source regions.

The two major events of flight F08 exhibit differences in the locations of their most recent PBL contacts. The first event is associated with air masses originating in the longitudinal range of 100–115°E while the second event is linked to air masses

230 from the 115–130°E region. Furthermore, the first event is more spatially constrained, occurring within the 30–40°N latitude band, whereas the second event encompasses a broader latitude range of around 20–40°N. The event observed during flight F17 illustrates an internal structure of CH_2Cl_2 mixing ratios with a maximum occurring approximately between 02:10 and 02:20 UTC. The calculations of FLEXPART suggest that the last contact of these air masses with the PBL was located over a wide range of longitudes but was restricted to a rather narrow latitudinal band around 30°N.

235 In both flights, the particles released within the 5-minute intervals in the shaded regions of Figure 3 and Figure 4 show the highest relative proportion of their respective 5-minute intervals that have reached the PBL within the 12 day time of our FLEXPART calculation (see Figures S 6 and S 7 in the SI). More specifically, during the first event, the proportions of particle trajectories that have reached the PBL within the prior 12 days are between 50% and 90%, while in the second event this figure ranges between 40% and 50%. In the F17 event, the relative share exceeds 40%, with occasional peaks between 60% and 80%,

240 which could indicate mixed air masses of different transport pathways. On isentropic levels similar to those associated with the three events, there exist time intervals during these flights where there is an increased percentage of trajectories that reach the PBL as well. However, these trajectories have lower percentages and different median latitudes and longitudes compared to the analyzed events. In the following, we examine the three major events in more depth.

3.3.1 Analysis of the last PBL contacts and the maximum updraft along the trajectories of the events

For each event, we combine the particle trajectories from the 5-minute intervals within the event duration, as dictated by the aforementioned conditions and represented by the red-shaded time ranges in Figures 3 and 4. The initial event occurred on August 26, 2023, from 19:25 to 20:05 UTC, featuring 40,000 particles. The following event on the same day spans from 20:25 to 21:15 UTC with 50,000 particles. The final event was observed on September 17, 2023, from 01:50 to 02:50 UTC, with 60,000 particles.

We not only looked at the last PBL contacts of each particle's path, but we also conducted an in-depth analysis of regions exhibiting the highest diabatic ascent rates to pinpoint areas of notable updraft along the particles' trajectories during these events. We followed the approach of Hanumanthu et al. (2020) and Lauther et al. (2022) to determine the maximum variation in potential temperature for each particle trajectory over an 18-hour period and report the central coordinates for these particles. The focus is on the spatial details of maximum rates along the backward trajectories of the particles rather than on their absolute values. To achieve this, we implemented a rolling window to aggregate the hourly changes in the potential temperature. To better illustrate the findings, the last PBL contacts and the maximum updraft within an 18-hour time frame ($\Delta\Theta_{18h}$) were binned into $2° \times 2°$ latitude-longitude intervals.

During the first event on flight F08 on August 26, 2023, almost 80% of the 40,000 particles (combined 5-minute intervals) reached the PBL during the 12 days. Most of the particle trajectories reached the PBL in the Huabei region of northern China, as well as parts of northwest China, including Gansu, Ningxia, and Qinghai provinces. Furthermore, some pathways extended to the far western part of northwest China, the tri-border area of Turkey, Iran, and Iraq, as well as the Pacific Ocean (Fig. 6 A). Transport times to the observation location, particularly from northern China, range from approximately 120 to 144 hours (5 to 6 days), with even shorter transport times simulated from trajectories originating in areas near the coast (Fig. 6 B). The most intense updrafts are found in northern China near the coastal areas of Hebei, Beijing, and Shanxi (Fig. 6 C and D).

Following the first event on flight F08, the second event was observed soon after, albeit at different isentropic levels. The pattern of the last PBL contacts and the maximum updraft differs somewhat from that of the first event, suggesting that different mechanisms are responsible for the transport. Approximately 40% of the 50,000 particles reached the PBL during the 12 days of calculation. The most recent PBL contacts are scattered across the Southeast and East Asia regions, as well as somewhat extending into the Pacific Ocean. However, a greater number of trajectories make their last PBL contacts in the Huadong region of East China and in Korea (Fig. 7 A) with transport times to the observation location ranging from approximately 120 to 168 hours (5 to 7 days). Two primary zones show the strongest updrafts along the trajectories: one dense area stretching from the Yangtze River Delta across the Yellow Sea, Korea, and into Russia's Primorje region, and another less concentrated, extending from Kamchatka southeastward over the Pacific Ocean (Fig. 7 C). Both regions exhibit comparable updraft intensities (Fig. 7 D).

The backward calculations for the event on flight F17 on September 17, 2023 displays another distinctive pattern of PBL contacts and strongest updrafts, compared to the two events on August 26, 2023. Approximately 60% of the 60,000 particles reached the PBL during the 12 days. Most of the particle trajectories reached the PBL in the more southerly regions of eastern

Asia, extending into southern and southeastern Asia. The most recent encounters are located in eastern Asia, particularly closer to the eastern coastal regions, occurring around 120 to 168 hours (5 to 7 days) before the flight (Fig. 8 A and B). The strongest updraft along the particle trajectories is predominantly confined to a narrow band that stretches from northern India along the southern border of the Tibetan Plateau, passing through Sichuan, Chongqing, Hubei, Anhui, and Jiangsu, and extending to Korea, with the intensity being more pronounced in the area around central to eastern China (Fig. 8 C and D).

3.3.2 Synoptic situations and vertical motions

We examined synoptic meteorological conditions that corresponded to the unique patterns of the back trajectories' last PBL contacts and maximum updrafts. ERA5 reanalysis data on pressure levels are provided on an hourly basis. For visualization purposes, only snapshots of the meteorological situation are given, e.g. times with large updrafts. The chosen times roughly coincide with the greatest updraft, based on time series of $\Delta\Theta$ (potential temperature variation along particle trajectories), visually represented using color codes according to latitude, longitude, and particle density (refer to Fig. S 8 to S 10 in the SI). Meteorological fields for periods exhibiting the greatest updrafts are also available in the SI (Fig. S 15 to S 20), together with airmass RGB satellite (EUMETSAT) images for the times of the snapshots (Fig. S 11 to S 13). Airmass RGB utilizes two water vapor and one ozone absorption channel to differentiate between air masses and high-altitude multi-layered clouds, supporting the examination of dynamic atmospheric processes.

The backward particle trajectories for the first event on flight F08 reveal multiple distinct occurrences of strong updrafts, the most substantial on August 22 and 23 (see Fig. S 8). Therefore, we examine two temporal snapshots as depicted in Figure 9. Figure 9 A presents a snapshot from August 22, 2023 10 UTC of the CAPE parameter. Located within the coordinates of approximately 110–118°E and 30–38°N is a region of enhanced CAPE, thus a region promoting strong and sustained upward air movement. The most substantial period of updraft is on August 23, 2023 19 UTC for which Figure 9 B shows the Q-Vector (arrows) and Q-Vector convergence (yellow to orange) and divergence (light to dark blue), together with the 500 hPa geopotential (black lines). Positioned at the peak of the updraft along the backward trajectories (see Fig. 6 D) is a zone of vertical upward motion, highlighted by the convergence of the Q-Vector. This is located downstream of a slightly negatively tilted 500 hPa trough, which gradually shifted east over the next few hours (not shown here). Furthermore, this area is located in the entrance region of an anticyclonically curved jetstreak (the 200 hPa wind is depicted in Fig. S 21 in the SI), which is related to the vertical upward movement in the troposphere. The closest RGB airmass satellite image at 18 UTC shows co-located high-level thick clouds (Fig. S 11).

For the second event on flight F08, the greatest updraft, noted in the majority of particles involved (Fig. 7 C), shows a distinct line from the Yangtze River Delta across the Yellow Sea, Korea, and into Russia's Primorje region. The peak period for the potential temperature gradient along the particles occurred from August 22 to early August 23, 2023 (see Fig. S 9). Since this appears to be a frontal structure, we utilize the thermal front parameter (TFP) for our investigation. Figure 10 A shows large TFP values (yellow to red shadings), located on the warm side of the thickness crowding zone (gradient range of the black lines from shallow to high thickness). This structure remained almost stationary from 22 August 2023 until the early hours of August 23, 2023. The Q-Vector convergence implies upward vertical motion for the region of the Yellow Sea, Korea, and

Russia's Primorje region (Fig. 10 B). Moreover, the 500 hPa geopotential chart reveals a detached upper-level low at around 120°E and 50°N. Consequently, this collectively indicates the potential presence of a frontal structure in this area. The RGB airmass satellite image supports this by showing a high-level thick band of clouds along the frontal zone with dark blue to brown colors (cold and dry air) on the rear side (Fig. S 12).

The event of flight F17 shows again a distinct line of maximum updraft from Korea, across China, and the southern border of the Tibetan Plateau (see Fig. 8 C and D). It is the only one of the three events that indicates an updraft in the SASM Monsoon Trough region and in the EASM. The Monsoon Trough region is accompanied by high CAPE values (see meteorological charts in SI). Although strong updraft events occur at several times during the period of the backward calculation, a substantial proportion of particles show their maximum upwind position on a very narrow line within 3 to 6 days prior to their release (see Fig 8 C and S 10). Aligned with the strongest updraft area in east China and Korea are large values of the TFP (Fig. 11 A), which begin to accumulate on September 12 and dissipate in the early hours of September 13, 2023. Fig 11 B illustrates consistent areas of upward vertical motion (Q-Vector convergence) near the positively tilted trough in that time. Much like the second event in flight F08, this frontal structure remains largely stationary throughout its duration. RGB airmass satellite image from September 12, 2023 at 21 UTC reveals a thick cloud band, co-located to large values of TFP (Fig. S 13).

3.4 Projected contribution to the stratosphere

All three events were observed in the upper troposphere around 330 to 350 K of potential temperature, in proximity to the tropopause and with tropospheric N_2O values (e.g. Fig. 3 A, 4 A, and S. 14). To find out whether these air masses with high CH_2Cl_2 can reach further into the stratosphere in the upcoming days, forward particle trajectories were generated. The procedure mirrored that of the backward trajectories, employing 5-minute intervals along the flight paths and combining intervals during the event durations. We classify the particle trajectories into three layers based on potential vorticity (potential vorticity unit; PVU). A specific PVU value for defining the dynamical tropopause is not universally established, but 2 PVU is a frequently used threshold (e.g. Holton et al., 1995). Kunz et al. (2009) described the layer where mixing occurs in the tropopause layer as the area that encompasses the dynamic tropopause and thermal tropopause, termed the "Tropospheric Freshly Mixed (TFM) branch". Furthermore, the lower limit of the TFM branch is established by the dynamical tropopause at 2 PVU, while the mean potential vorticity at the thermal tropopause is estimated to be around 4 PVU. Taking this into account, we utilize the following classification: The first layer is assigned to potential vorticity values below 2 PVU, indicating that it is in the troposphere. The second layer is assigned to values ranging from 2 to 4 PVU, which identifies it as the tropopause layer. The third layer, with values exceeding 4 PVU, is classified as stratospheric. Table 1 shows the percentage share of the ranges 2-4 PVU and greater than 4 PVU (the remaining percentage is below 2 PVU), averaged over 48-hour intervals.

All three events demonstrate comparable slight increases in the stratospheric portion with time (> 4 PVU) and exhibit more variations in the share within the tropopause layer (2–4 PVU). In addition, the first event on flight F08 is the only one that shows a minor presence of particles in the tropopause layer and stratosphere within the first 48 h after release.

The first event on flight F08 indicates a minor presence of the particles in the tropopause layer with a decrease within the following days. For the second event on flight F08, the largest share in the tropopause layer was within 7 to 8 days after release

with up to 8.9% with a decreasing contribution afterwards, probably due to the return of some particles to the free troposphere. The largest share to the tropopause layer can be seen for the event on fight F17 with up to 27.6% on days 5 and 6 with a decreased share in the following days.

The proportion in the stratosphere increases within the 12 days of forward calculation to around 2.4% and 3.8% for the three events. For the event on flight F08, the stratospheric proportion exists from the beginning and peaks at 3.8% after 5 to 6 days. In contrast, for the second event on flight F08 and the event on flight F17, the stratospheric share starts 5 to 6 days after release, reaching its peaks at 2. 4% and 3. 2%, respectively, after 11 to 12 days. The steady increase of particles in the stratosphere within the 12 days could possibly continue in the following days.

4 Discussion

CH_2Cl_2 mixing ratios of up to 300 ppt were observed in the upper troposphere (11–12.5 km) above Alaska and the Gulf of Alaska region. For comparison, observations during take-off and landing at Anchorage show CH_2Cl_2 mixing ratios of about 60 ppt near the ground (see Fig. 3 and 4). We were able to assign the origin of these large mixing ratios to the region of the ASM. We were not the first to observe elevated mixing ratios of CH_2Cl_2 in the upper troposphere, although the focus of previous studies was predominantly on measurements within the ASM or transport in a tropical direction. For instance, Oram et al. (2017) detected CH_2Cl_2 mixing ratios as high as 121 ppt in the upper troposphere (10–12 km) over the Bay of Bengal, originating from East Asia and with potential for transport into the tropical regions of the western Pacific, eventually rising to the tropical upper troposphere. Treadaway et al. (2022) investigated the transport of Asian emissions to the tropical tropopause layer of the West Pacific with a plume of around 90 ppt CH_2Cl_2 (at 14–16 km) with air that originated predominantly from India. Adcock et al. (2021) found tropopause mixing ratios of CH_2Cl_2 in the range of 65–136 ppt in the tropopause region and indicated possible source regions in South Asia. All these studies show enhanced values of CH_2Cl_2 in the upper troposphere and tropopause region, but do not reach the values we observed in the upper troposphere in the subarctic area of Alaska. Furthermore, the focus of these studies is on the tropical uplift of elevated CH_2Cl_2 and potential sources from India and South to East Asia. This study mainly examines elevated CH_2Cl_2 mixing ratios originating in the EASM region, which were transported to higher latitudes over longer distances. Caution is advised when comparing the absolute values of CH_2Cl_2 with earlier studies, as there has been a notable increase in CH_2Cl_2 emissions over the past decade, rising by a factor of 2.5 (Laube and Tegtmeier, 2022). However, it is clear that the increase in emissions in the region of the EASM is developing much more strongly with considerable importance for transport into the upper troposphere and lower stratosphere.

A more recent study by Pan et al. (2024) not only provides additional evidence for SASM injection of short-lived ozone depleting substances, but also highlights the key role of EASM in injection into the stratosphere. During the ACCLIP campaign, an unusual northward shift of the convergence zone was observed due to an atypical configuration of the ASM for that year. Typically, the convergence zone is positioned slightly more southward. However, both in 2022 and climatologically, the convergence zone intersects with significant Cl-VSLS sources along the coastal regions of East Asia (Pan et al., 2024).

Our findings support this statement, as our backward trajectories for three substantial CH_2Cl_2 plume observations in the upper troposphere revealed the last PBL contacts in known source areas of CH_2Cl_2 and peak updrafts suggest predominantly typical line structures, which can be associated with frontal structures and convergence zones (also visible in RGB airmass satellite images in the SI). This highlights once more the importance of viewing the EASM as a key pathway for transporting Cl-VSLS into the upper troposphere, thereby contributing to an increase in tropospheric background levels with the potential to enter the lower stratosphere. Moreover, the transport times and areas of increased CH_2Cl_2 mixing ratios shown here suggest that transport to the upper troposphere in the subarctic region is driven by large convective transport contributions from the EASM. Previous studies have focused more on the entry of polluted air into the UTLS via the ASMA with subsequent eddy shedding events. The ASMA covers a range of potential temperatures from approximately 360–450 K (see, for example, Vogel et al., 2019). Small-scale eddies are shed from the main anticyclone (i.e. the so-called eddy shedding events) with quasi-horizontal isentropic transport out of the anticyclone, either directly into the lower stratosphere or into the tropical troposphere with subsequent slower transport into the stratosphere (e.g. Clemens et al., 2022). Elevated CH_2Cl_2 mixing ratios were identified in a potential temperature range of 330–350 K in this study, thus below the ASMA.

Typical frontal structures in the EASM region include the Meiyu, Baiu, and Changma fronts, where the name changes with the location of the frontal structure. As the monsoon progresses, the structures shift northward. They first appear over Taiwan, southern China, and the Okinawa region from early May to mid-June. They then move to the Yangtze River valley and the main islands of Japan from mid-June to mid-July, and finally reach the Korean Peninsula and northeast China during mid-July to mid-August (e.g. Jun-Mei et al., 2013). In this study, frontal structures were observed at the end of August. Shin et al. (2022) investigated the synoptic characteristics of the quasi-stationary front of August 26-27 2018 over the Korean peninsula, similar to the frontal structure within this study. The quasi-stationary front observed in their study exhibited features similar to the Changma front. The environmental conditions of the August event examined were atypical for heavy rainfall with a quasi-stationary front and are closely related to the expansion of the subtropical high of the west Pacific (WPSH) (Shin et al., 2022). This study also observed an expansion of the WPSH, occurring not just in late August but also in mid-September accompanied by frontal structures.

We conducted a preliminary analysis of the potential for elevated CH_2Cl_2 occurrences to penetrate deeper into the tropopause layer and lower stratosphere. The ongoing challenge is to mitigate stratospheric ozone depletion caused by the increasing trend of uncontrolled Cl-VSLS (Chipperfield and Bekki, 2024). The forward trajectory analysis indicates varied contributions for the three events. For the tropopause layer, the contribution fluctuated significantly between events, reaching approximately 25% during the largest event. All three events show a minor contribution to the lower stratosphere up to about 3.8% within the 12-day period following the events. We are considering a specific time frame and geographic region, while other regions may have a greater impact on transportation into the stratosphere. For instance, transport can occur in the ridges of baroclinic waves on the anticyclonic side of the jet stream, situated above the outflow of warm conveyor belts (e.g. Kunkel et al., 2019).

5 Summary and Conclusion

We report on measurements of CH_2Cl_2 from two in situ instruments and N_2O from a third in situ instrument during the HALO aircraft campaign PHILEAS in late summer 2023. One of the primary scientific interests centered on how polluted air from the Asian Summer Monsoon region reached the extratropical upper troposphere and lower stratosphere (UTLS), with research flights mainly originating from Anchorage, Alaska. In addition, the FLEXPART Lagrangian dispersion model was used to investigate the origin of selected pollution events, the corresponding transport times from the planetary boundary layer (PBL), and the potential for further input into the lower stratosphere, using calculations extending 12 days both backward and forward.

The measurements of CH_2Cl_2 recorded by the two in situ instruments align very well. Major pollution events during the PHILEAS campaign were identified by examining the relationship between CH_2Cl_2 and N_2O. Two flights (F08 and F17) showed three very clear events with CH_2Cl_2 mixing ratios of 200 to 300 ppt at altitudes of about 11 to 12.5 km and 330 to 350 K potential temperature over the northwestern Pacific up to the subarctic region of Alaska. These mixing ratios deviate substantially from the comparable median mixing ratios of the campaign.

The FLEXPART model in backward mode was used to trace the origins and transport times of air masses responsible for elevated mixing ratios observed during the aforementioned pollution events. For each event, the paths of the computational air particles were analyzed to identify the last planetary boundary layer (PBL) contacts and regions of maximum diabatic ascent using potential temperature variations along particle trajectories. Transport times between PBL and the flight paths for the three events were around 5-7 days. For the first event in flight F08, the particle trajectories reached the PBL primarily over northern China (approximately 100-115° E and 30-40° N), with updrafts focused closer to coastal areas. For the second event in flight F08, the particle trajectories, which reached the PBL, dispersed across Southeast and East Asia (approximately 115-130° E and 20-40° N). The updrafts were notably strong along the Yangtze River Delta, Korea, and extending into Russia. For the event on flight F17, the particle trajectories reached the PBL in broader region of southern to southeastern Asia (approximately 80-120° E and 20-30° N). Updrafts were concentrated from northern India to eastern China and Korea.

ERA5 reanalysis was used to identify meteorological conditions, such as frontal structures and vertical motions that aligned with particle trajectory patterns and updraft intensities. Key findings indicated distinct patterns in each event, influenced by regional meteorological conditions such as convective areas and frontal structures, revealed through parameters such as CAPE, Q-Vector divergence, and the thermal front parameter (TFP). RGB airmass satellite images were used to confirm the presence of frontal structure with associated cloud formations.

This analysis of the elevated CH_2Cl_2 mixing ratios indicates that the transport into the upper troposphere in the subarctic region resulted from convective upwelling by the EASM and subsequent displacement over the northern Pacific Ocean before the air masses could ascent further into the ASMA and were subsequently transported into the lower stratosphere.

By forward FLEXPART calculation of the three events, the potential of these observed elevated CH_2Cl_2 mixing ratios to reach the tropopause layer and lower stratosphere in the following days (12-day time period) was investigated. Even if a substantial proportion reaches the tropopause layer (up to 27.6% for flight F17), the contribution to the lower stratosphere is minor for all three events (1.3% to 3.8%). However, it remains unclear whether this observation is limited to the events we

observed or if it extends more generally to convection within the East Asian part of the monsoon circulation. More detailed

445 and systematical investigation is needed to determine this.

Data availability. The observational data of the HALO flights during the PHILEAS campaign are available via the HALO database (https://halo-db.pa.op.dlr.de) or upon request from the main author. The calculation of the FLEXPART model is available upon request.

Author contributions. MJ, TK, TS, and AE operated and provided data of the GhOST instrument; VL, RVL, JS, and CMV operated and provided data of the HAGAR-V instrument; NE, FW, HCL, and PH operated and provided data of the UMAQS instrument; MJ did the

450 FLEXPART simulations. MJ performed the data analysis and wrote the paper. All authors have contributed via discussions and comments.

Competing interests. At least one of the (co-)authors is a member of the editorial board of Atmospheric Chemistry and Physics

Acknowledgements. This work was done at the University of Frankfurt. The authors thank the DLR staff for the operation of the HALO and the support during the campaign, and also the coordinators and colleagues for productive cooperation during the campaign. This research was supported by the German Research Foundation (DFG) within the Priority Program HALO SSP 1294 under the number 316646266. This

455 work was funded by the DFG collaborative research program "The Tropopause Region in a Changing Atmosphere" TRR 301 – project ID 428312742.

References

Adcock, K. E., Fraser, P. J., Hall, B. D., Langenfelds, R. L., Lee, G., Montzka, S. A., Oram, D. E., Röckmann, T., Stroh, F., Sturges, W. T., Vogel, B., and Laube, J. C.: Aircraft-Based Observations of Ozone-Depleting Substances in the Upper Troposphere and Lower Stratosphere in and Above the Asian Summer Monsoon, Journal of Geophysical Research: Atmospheres, 126, e2020JD033 137, https://doi.org/https://doi.org/10.1029/2020JD033137, e2020JD033137 2020JD033137, 2021.

An, M., Western, L. M., Say, D., Chen, L., Claxton, T., Ganesan, A. L., Hossaini, R., Krummel, P. B., Manning, A. J., Mühle, J., O'Doherty, S., Prinn, R. G., Weiss, R. F., Young, D., Hu, J., Yao, B., and Rigby, M.: Rapid increase in dichloromethane emissions from China inferred through atmospheric observations, Nature Communications, 12, https://doi.org/10.1038/s41467-021-27592-y, 2021.

Arnold, T., Mühle, J., Salameh, P. K., Harth, C. M., Ivy, D. J., and Weiss, R. F.: Automated Measurement of Nitrogen Trifluoride in Ambient Air, Analytical Chemistry, 84, 4798–4804, https://doi.org/10.1021/ac300373e, 2012.

Bakels, L., Tatsii, D., Tipka, A., Thompson, R., Dütsch, M., Blaschek, M., Seibert, P., Baier, K., Bucci, S., Cassiani, M., Eckhardt, S., Groot Zwaaftink, C., Henne, S., Kaufmann, P., Lechner, V., Maurer, C., Mulder, M. D., Pisso, I., Plach, A., Subramanian, R., Vojta, M., and Stohl, A.: FLEXPART version 11: improved accuracy, efficiency, and flexibility, Geoscientific Model Development, 17, 7595–7627, https://doi.org/10.5194/gmd-17-7595-2024, 2024.

Bednarz, E. M., Hossaini, R., and Chipperfield, M. P.: Atmospheric impacts of chlorinated very short-lived substances over the recent past – Part 2: Impacts on ozone, Atmospheric Chemistry and Physics, 23, 13 701–13 711, https://doi.org/10.5194/acp-23-13701-2023, 2023.

Bluestein, H. B.: Synoptic-dynamic meteorology in midlatitudes: Volume I: Principles of kinematics and dynamics, Synoptic-Dynamic Meteorology in Midlatitudes, Oxford University Press, New York, NY, 1992.

Burkholder, J. B., Hodnebrog, O., McDonald, B. C., Orkin, V., Papadimitriou, V. C., and Hoomissen, D. V.: Annex: Summary of Abundance, Lifetimes, ODPs, REs, GWPs, and GTPs, 278, World Meteorological Organization, Geneva, Switzerland, 2022.

Cassiani, M., Stohl, A., and Brioude, J.: Lagrangian Stochastic Modelling of Dispersion in the Convective Boundary Layer with Skewed Turbulence Conditions and a Vertical Density Gradient: Formulation and Implementation in the FLEXPART Model, Boundary-Layer Meteorology, 154, 367–390, https://doi.org/10.1007/s10546-014-9976-5, 2015.

Chipperfield, M. P. and Bekki, S.: Opinion: Stratospheric ozone – depletion, recovery and new challenges, Atmospheric Chemistry and Physics, 24, 2783–2802, https://doi.org/10.5194/acp-24-2783-2024, 2024.

Claxton, T., Hossaini, R., Wilson, C., Montzka, S. A., Chipperfield, M. P., Wild, O., Bednarz, E. M., Carpenter, L. J., Andrews, S. J., Hackenberg, S. C., Mühle, J., Oram, D., Park, S., Park, M.-K., Atlas, E., Navarro, M., Schauffler, S., Sherry, D., Vollmer, M., Schuck, T., Engel, A., Krummel, P. B., Maione, M., Arduini, J., Saito, T., Yokouchi, Y., O'Doherty, S., Young, D., and Lunder, C.: A Synthesis Inversion to Constrain Global Emissions of Two Very Short Lived Chlorocarbons: Dichloromethane, and Perchloroethylene, Journal of Geophysical Research: Atmospheres, 125, e2019JD031 818, https://doi.org/https://doi.org/10.1029/2019JD031818, e2019JD031818 2019JD031818, 2020.

Clemens, J., Ploeger, F., Konopka, P., Portmann, R., Sprenger, M., and Wernli, H.: Characterization of transport from the Asian summer monsoon anticyclone into the UTLS via shedding of low potential vorticity cutoffs, Atmospheric Chemistry and Physics, 22, 3841–3860, https://doi.org/10.5194/acp-22-3841-2022, 2022.

Copernicus Climate Change Service: ERA5 hourly data on pressure levels from 1940 to present, https://doi.org/10.24381/CDS.BD0915C6, 2018.

Emanuel, K. A. and Živković Rothman, M.: Development and Evaluation of a Convection Scheme for Use in Climate Models, Journal of the Atmospheric Sciences, 56, 1766 – 1782, https://doi.org/10.1175/1520-0469(1999)056<1766:DAEOAC>2.0.CO;2, 1999.

495 Garny, H. and Randel, W. J.: Transport pathways from the Asian monsoon anticyclone to the stratosphere, Atmospheric Chemistry and Physics, 16, 2703–2718, https://doi.org/10.5194/acp-16-2703-2016, 2016.

Ha, K.-J., Seo, Y.-W., Lee, J.-Y., Kripalani, R. H., and Yun, K.-S.: Linkages between the South and East Asian summer monsoons: a review and revisit, Climate Dynamics, 51, 4207–4227, https://doi.org/10.1007/s00382-017-3773-z, 2017.

Hanna, S. R.: Applications in Air Pollution Modeling, pp. 275–310, Springer Netherlands, Dordrecht, https://doi.org/10.1007/978-94-010-9112-1_7, 1982.

500

Hanumanthu, S., Vogel, B., Müller, R., Brunamonti, S., Fadnavis, S., Li, D., Ölsner, P., Naja, M., Singh, B. B., Kumar, K. R., Sonbawne, S., Jauhiainen, H., Vömel, H., Luo, B., Jorge, T., Wienhold, F. G., Dirkson, R., and Peter, T.: Strong day-to-day variability of the Asian Tropopause Aerosol Layer (ATAL) in August 2016 at the Himalayan foothills, Atmospheric Chemistry and Physics, 20, 14 273–14 302, https://doi.org/10.5194/acp-20-14273-2020, 2020.

505 Hersbach, H., Bell, B., Berrisford, P., Hirahara, S., Horányi, A., Muñoz-Sabater, J., Nicolas, J., Peubey, C., Radu, R., Schepers, D., Simmons, A., Soci, C., Abdalla, S., Abellan, X., Balsamo, G., Bechtold, P., Biavati, G., Bidlot, J., Bonavita, M., De Chiara, G., Dahlgren, P., Dee, D., Diamantakis, M., Dragani, R., Flemming, J., Forbes, R., Fuentes, M., Geer, A., Haimberger, L., Healy, S., Hogan, R. J., Hólm, E., Janisková, M., Keeley, S., Laloyaux, P., Lopez, P., Lupu, C., Radnoti, G., de Rosnay, P., Rozum, I., Vamborg, F., Villaume, S., and Thépaut, J.-N.: The ERA5 global reanalysis, Quarterly Journal of the Royal Meteorological Society, 146, 1999–2049,

510 https://doi.org/https://doi.org/10.1002/qj.3803, 2020.

Hewson, T. D.: Objective fronts., 1998.

Hofmann, H., Kafadar, K., and Wickham, H.: Letter-value plots: Boxplots for large data, Tech. rep., had.co.nz, 2011.

Holton, J. R., Haynes, P. H., McIntyre, M. E., Douglass, A. R., Rood, R. B., and Pfister, L.: Stratosphere-troposphere exchange, Reviews of Geophysics, 33, 403–439, https://doi.org/https://doi.org/10.1029/95RG02097, 1995.

515 Hoskins, B. J., Draghici, I., and Davies, H. C.: A new look at the ω-equation, Quarterly Journal of the Royal Meteorological Society, 104, 31–38, https://doi.org/https://doi.org/10.1002/qj.49710443903, 1978.

Hossaini, R., Chipperfield, M. P., Montzka, S. A., Leeson, A. A., Dhomse, S. S., and Pyle, J. A.: The increasing threat to stratospheric ozone from dichloromethane, Nature Communications, 8, https://doi.org/10.1038/ncomms15962, 2017.

Jesswein, M., Bozem, H., Lachnitt, H.-C., Hoor, P., Wagenhäuser, T., Keber, T., Schuck, T., and Engel, A.: Comparison of inorganic chlorine

520 in the Antarctic and Arctic lowermost stratosphere by separate late winter aircraft measurements, Atmospheric Chemistry and Physics, 21, 17 225–17 241, https://doi.org/10.5194/acp-21-17225-2021, 2021.

Jun-Mei, L., Jian-Hua, J., and Shi-Yan, T.: Re-Discussion on East Asian Meiyu Rainy Season, Atmospheric and Oceanic Science Letters, 6, 279–283, https://doi.org/10.3878/j.issn.1674-2834.13.0024, 2013.

Keber, T., Bönisch, H., Hartick, C., Hauck, M., Lefrancois, F., Obersteiner, F., Ringsdorf, A., Schohl, N., Schuck, T., Hossaini, R., Graf, P.,

525 Jöckel, P., and Engel, A.: Bromine from short-lived source gases in the extratropical northern hemispheric upper troposphere and lower stratosphere (UTLS), Atmospheric Chemistry and Physics, 20, 4105–4132, https://doi.org/10.5194/acp-20-4105-2020, 2020.

Kitabatake, N.: Extratropical Transition of Tropical Cyclones in the Western North Pacific: Their Frontal Evolution, Monthly Weather Review, 136, 2066 – 2090, https://doi.org/10.1175/2007MWR1958.1, 2008.

Krautstrunk, M. and Giez, A.: The Transition From FALCON to HALO Era Airborne Atmospheric Research, pp. 609–624, Springer Berlin

530 Heidelberg, Berlin, Heidelberg, https://doi.org/10.1007/978-3-642-30183-4_37, 2012.

Kunkel, D., Hoor, P., Kaluza, T., Ungermann, J., Kluschat, B., Giez, A., Lachnitt, H.-C., Kaufmann, M., and Riese, M.: Evidence of small-scale quasi-isentropic mixing in ridges of extratropical baroclinic waves, Atmospheric Chemistry and Physics, 19, 12 607–12 630, https://doi.org/10.5194/acp-19-12607-2019, 2019.

535 Kunz, A., Konopka, P., Müller, R., Pan, L. L., Schiller, C., and Rohrer, F.: High static stability in the mixing layer above the extratropical tropopause, Journal of Geophysical Research: Atmospheres, 114, https://doi.org/https://doi.org/10.1029/2009JD011840, 2009.

Lackmann, G.: Midlatitude synoptic meteorology – dynamics, analysis, and forecasting, American Meteorological Society, Boston, MA, 2011.

Laube, J. C., Tegtmeier, S., Fernandez, R. P., Harrison, J., L.Hu, Krummel, P., Mahieu, E., Park, S., and Western, L.: Update on Ozone-Depletion Substances (ODSs) and other Gases of Interest to the Montreal Protocol, chap. 1, 278, World Meteorological Organization,

540 Geneva, Switzerland, 2022.

Lauther, V., Vogel, B., Wintel, J., Rau, A., Hoor, P., Bense, V., Müller, R., and Volk, C. M.: In situ observations of CH_2Cl_2 and $CHCl_3$ show efficient transport pathways for very short-lived species into the lower stratosphere via the Asian and the North American summer monsoon, Atmospheric Chemistry and Physics, 22, 2049–2077, https://doi.org/10.5194/acp-22-2049-2022, 2022.

Legras, B., Joseph, B., and Lefèvre, F.: Vertical diffusivity in the lower stratosphere from Lagrangian back-trajectory reconstructions of

545 ozone profiles, Journal of Geophysical Research: Atmospheres, 108, https://doi.org/https://doi.org/10.1029/2002JD003045, 2003.

Li, T., Wang, Y., Wang, B., Ting, M., Ding, Y., Sun, Y., He, C., and Yang, G.: Distinctive South and East Asian monsoon circulation responses to global warming, Science Bulletin, 67, 762–770, https://doi.org/https://doi.org/10.1016/j.scib.2021.12.001, 2022.

Miller, B. R., Weiss, R. F., Salameh, P. K., Tanhua, T., Greally, B. R., Mühle, J., and Simmonds, P. G.: Medusa: A Sample Preconcentration and GC/MS Detector System for in Situ Measurements of Atmospheric Trace Halocarbons, Hydrocarbons, and Sulfur Compounds,

550 Analytical Chemistry, 80, 1536–1545, https://doi.org/10.1021/ac702084k, 2008.

Montzka, S., Reimann, S., Engel, A., Krüger, K., O'Doherty, S., and Sturges, W.: Ozone-Depleting Substances (ODSs) and Related Chemicals, pp. 1 – 112, World Meteorological Organization, Geneva, Switzerland, 2010.

Müller, S., Hoor, P., Berkes, F., Bozem, H., Klingebiel, M., Reutter, P., Smit, H. G. J., Wendisch, M., Spichtinger, P., and Borrmann, S.: In situ detection of stratosphere-troposphere exchange of cirrus particles in the midlatitudes, Geophysical Research Letters, 42, 949–955,

555 https://doi.org/https://doi.org/10.1002/2014GL062556, 2015.

Oram, D. E., Ashfold, M. J., Laube, J. C., Gooch, L. J., Humphrey, S., Sturges, W. T., Leedham Elvidge, E. C., Forster, G. L., Harris, N. R. P., Mead, M. I., Samah, A. A., Phang, S. M., Ou-Yang, C.-F., Lin, N.-H., Wang, J.-L., Baker, A. K., Brenninkmeijer, C. A. M., and Sherry, D.: A growing threat to the ozone layer from short-lived anthropogenic chlorocarbons, Atmospheric Chemistry and Physics, 17, 11 929–11 941, https://doi.org/10.5194/acp-17-11929-2017, 2017.

560 Pan, L. L., Honomichl, S. B., Kinnison, D. E., Abalos, M., Randel, W. J., Bergman, J. W., and Bian, J.: Transport of chemical tracers from the boundary layer to stratosphere associated with the dynamics of the Asian summer monsoon, Journal of Geophysical Research: Atmospheres, 121, 14,159–14,174, https://doi.org/https://doi.org/10.1002/2016JD025616, 2016.

Pan, L. L., Kinnison, D., Liang, Q., Chin, M., Santee, M. L., Flemming, J., Smith, W. P., Honomichl, S. B., Bresch, J. F., Lait, L. R., Zhu, Y., Tilmes, S., Colarco, P. R., Warner, J., Vuvan, A., Clerbaux, C., Atlas, E. L., Newman, P. A., Thornberry, T., Randel, W. J., and Toon, O. B.:

565 A Multimodel Investigation of Asian Summer Monsoon UTLS Transport Over the Western Pacific, Journal of Geophysical Research: Atmospheres, 127, e2022JD037 511, https://doi.org/https://doi.org/10.1029/2022JD037511, e2022JD037511 2022JD037511, 2022.

Pan, L. L., Atlas, E. L., Honomichl, S. B., Smith, W. P., Kinnison, D. E., Solomon, S., Santee, M. L., Saiz-Lopez, A., Laube, J. C., Wang, B., Ueyama, R., Bresch, J. F., Hornbrook, R. S., Apel, E. C., Hills, A. J., Treadaway, V., Smith, K., Schauffler, S., Donnelly, S., Hendershot, R.,

Lueb, R., Campos, T., Viciani, S., D'Amato, F., Bianchini, G., Barucci, M., Podolske, J. R., Iraci, L. T., Gurganus, C., Bui, P., Dean-Day, J. M., Millán, L., Ryoo, J.-M., Barletta, B., Koo, J.-H., Kim, J., Liang, Q., Randel, W. J., Thornberry, T., and Newman, P. A.: East Asian summer monsoon delivers large abundances of very short-lived organic chlorine substances to the lower stratosphere, Proceedings of the National Academy of Sciences, 121, e2318716 121, https://doi.org/10.1073/pnas.2318716121, 2024.

Park, M., Randel, W. J., Gettelman, A., Massie, S. T., and Jiang, J. H.: Transport above the Asian summer monsoon anticyclone inferred from Aura Microwave Limb Sounder tracers, Journal of Geophysical Research: Atmospheres, 112, https://doi.org/https://doi.org/10.1029/2006JD008294, 2007.

Pisso, I., Sollum, E., Grythe, H., Kristiansen, N. I., Cassiani, M., Eckhardt, S., Arnold, D., Morton, D., Thompson, R. L., Groot Zwaaftink, C. D., Evangeliou, N., Sodemann, H., Haimberger, L., Henne, S., Brunner, D., Burkhart, J. F., Fouilloux, A., Brioude, J., Philipp, A., Seibert, P., and Stohl, A.: The Lagrangian particle dispersion model FLEXPART version 10.4, Geoscientific Model Development, 12, 4955–4997, https://doi.org/10.5194/gmd-12-4955-2019, 2019.

Ploeger, F., Gottschling, C., Griessbach, S., Grooß, J.-U., Guenther, G., Konopka, P., Müller, R., Riese, M., Stroh, F., Tao, M., Ungermann, J., Vogel, B., and von Hobe, M.: A potential vorticity-based determination of the transport barrier in the Asian summer monsoon anticyclone, Atmospheric Chemistry and Physics, 15, 13 145–13 159, https://doi.org/10.5194/acp-15-13145-2015, 2015.

Prather, M. J., Hsu, J., DeLuca, N. M., Jackman, C. H., Oman, L. D., Douglass, A. R., Fleming, E. L., Strahan, S. E., Steenrod, S. D., Søvde, O. A., Isaksen, I. S. A., Froidevaux, L., and Funke, B.: Measuring and modeling the lifetime of nitrous oxide including its variability, Journal of Geophysical Research: Atmospheres, 120, 5693–5705, https://doi.org/https://doi.org/10.1002/2015JD023267, 2015.

Renard, R. J. and Clarke, L. C.: Experiments in numerical objective frontal analysis., 1965.

Riese, M., Hoor, P., Kunkel, D., Vogel, B., Kachula, O., Ploeger, F., Clemens, J., Geldenhuys, M., Guenther, G., Borrmann, S., Engel, A., Fadnavis, S., Friedl-Vallon, F., Grooß, J. U., Hegglin, M. I., Hoepfner, M., Jesswein, M., Johansson, S., Kaumanns, J., Koellner, F., Lauther, V., Mueller, R., Poehlker, M., Rapp, M., Rhode, S., Schneider, J., Schuck, T., Sinnhuber B. M. Tomsche, L., von Hobe, M., Ungermann, J., Versick, S., Voigt, C., Volk, M., Zahn, A., and Ziereis, H.: Long-range transport of polluted Asian summer monsoon air to high latitudes during the PHILEAS campaign in the boreal summer 2023, submitted, 2025.

Ryall, D. and Maryon, R.: Validation of the UK Met. Office's name model against the ETEX dataset, Atmospheric Environment, 32, 4265–4276, https://doi.org/https://doi.org/10.1016/S1352-2310(98)00177-0, 1998.

Schuck, T. J., Lefrancois, F., Gallmann, F., Wang, D., Jesswein, M., Hoker, J., Bönisch, H., and Engel, A.: Establishing long-term measurements of halocarbons at Taunus Observatory, Atmospheric Chemistry and Physics, 18, 16 553–16 569, https://doi.org/10.5194/acp-18-16553-2018, 2018.

Shin, U., Park, S.-H., Yun, Y.-R., and Oh, C.: Synoptic Features of August Heavy Rainfall Episodes Accompanied By a Quasi-Stationary Front Over the Korean Peninsula and Its Relationship With the Western Pacific Subtropical High, Frontiers in Earth Science, 10, https://doi.org/10.3389/feart.2022.940785, 2022.

Stohl, A., Hittenberger, M., and Wotawa, G.: Validation of the lagrangian particle dispersion model flexpart against large-scale tracer experiment data, Atmospheric Environment, 32, 4245–4264, 1998.

Stohl, A., Forster, C., Frank, A., Seibert, P., and Wotawa, G.: Technical note: The Lagrangian particle dispersion model FLEXPART version 6.2, Atmospheric Chemistry and Physics, 5, 2461–2474, https://doi.org/10.5194/acp-5-2461-2005, 2005.

Treadaway, V., Atlas, E., Schauffler, S., Navarro, M., Ueyama, R., Pfister, L., Thornberry, T., Rollins, A., Elkins, J., Moore, F., and Rosenlof, K.: Long-range transport of Asian emissions to the West Pacific tropical tropopause layer, Journal of Atmospheric Chemistry, 79, 81–100, https://doi.org/10.1007/s10874-022-09430-7, 2022.

Vogel, B., Müller, R., Günther, G., Spang, R., Hanumanthu, S., Li, D., Riese, M., and Stiller, G. P.: Lagrangian simulations of the transport of young air masses to the top of the Asian monsoon anticyclone and into the tropical pipe, Atmospheric Chemistry and Physics, 19, 6007–6034, https://doi.org/10.5194/acp-19-6007-2019, 2019.

610 World Meteorological Organization: State of the climate in Asia 2023, United Nations, https://www.uncclearn.org/wp-content/uploads/library/1350_State-of-the-Climate-in-Asia-2023.pdf, 2024.
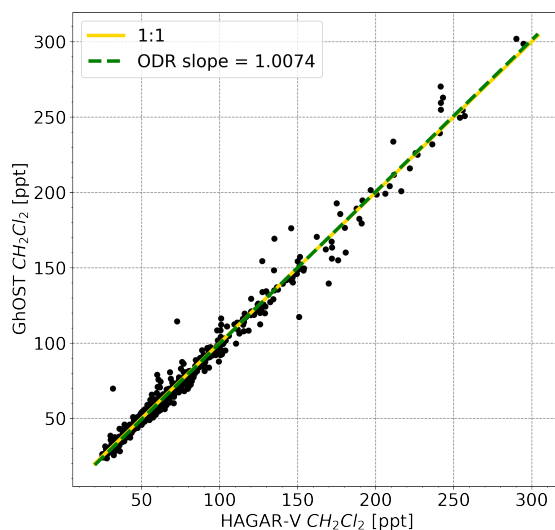
Figure 1. Correlation of CH_2Cl_2 measured with the HAGAR-V instrument (x-axis) and the GhOST instrument (y-axis). HAGAR-V measurements were averaged when more than one observation is within the sample time of the GhOST instrument. The 1-to-1 line is shown in yellow (solid) and the slope of the orthogonal distance regression is shown in green (dashed)
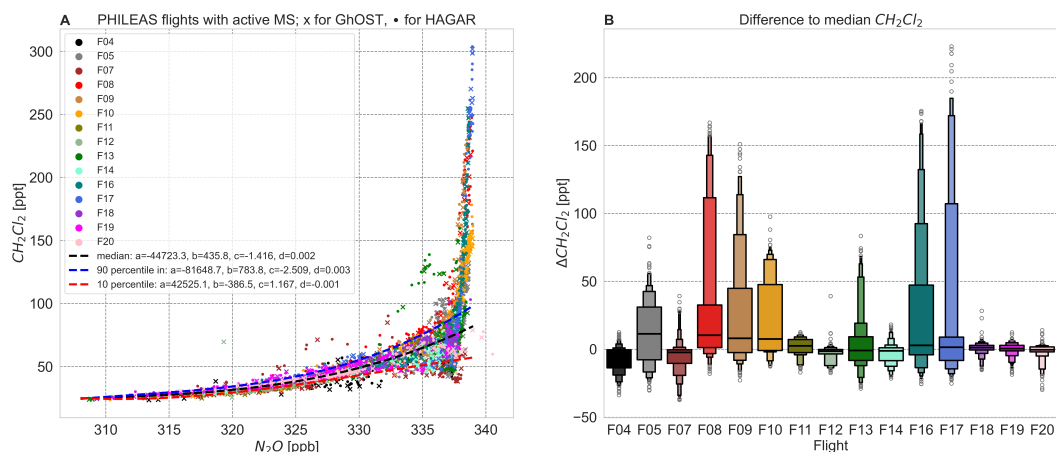
Figure 2. A CH_2Cl_2-N_2O relationship, color coded by flight. Crosses for HAGAR-V and points for GhOST. N_2O is averaged to the respective sample enrichment time of the gas chromatographs. Black dashed curve indicates median curve fit, blue and red dashed line the 90th and 10th percentile curve fits. **B** Letter-value plots of ΔCH_2Cl_2 for every PHILEAS flight to median CH_2Cl_2 value derived from median curve fit. Horizontal lines show median and points extreme outliers.
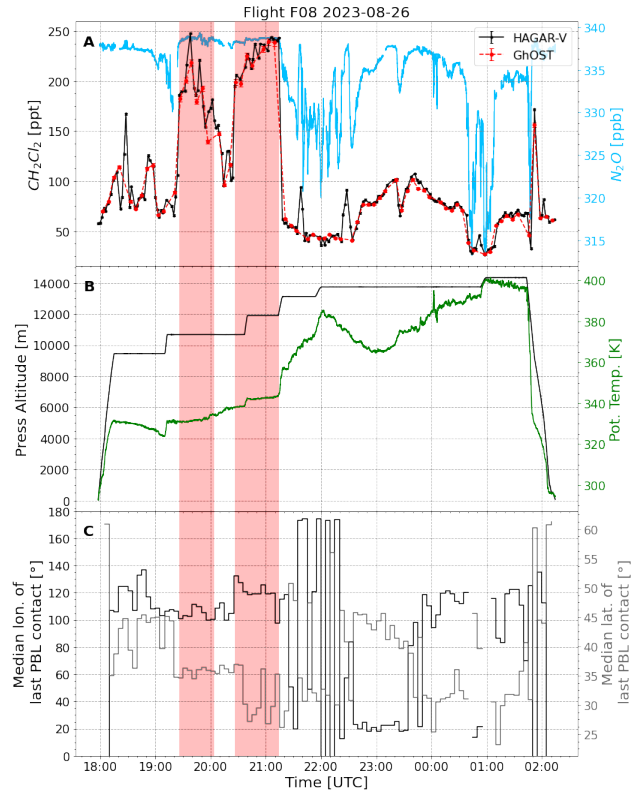
Figure 3. A Time series of flight F08 on August 26, 2023. Mixing ratios of CH$_2$Cl$_2$ of the GhOST in red and HAGAR-V in black (left y-axis) and N$_2$O in blue (right y-axis). **B** Pressure altitude in black and potential temperature in green along the flight path. **C** FLEXPART median latitude in grey and longitude in black of particles within the 5-min intervals. Major elevated time ranges are highlighted in red.
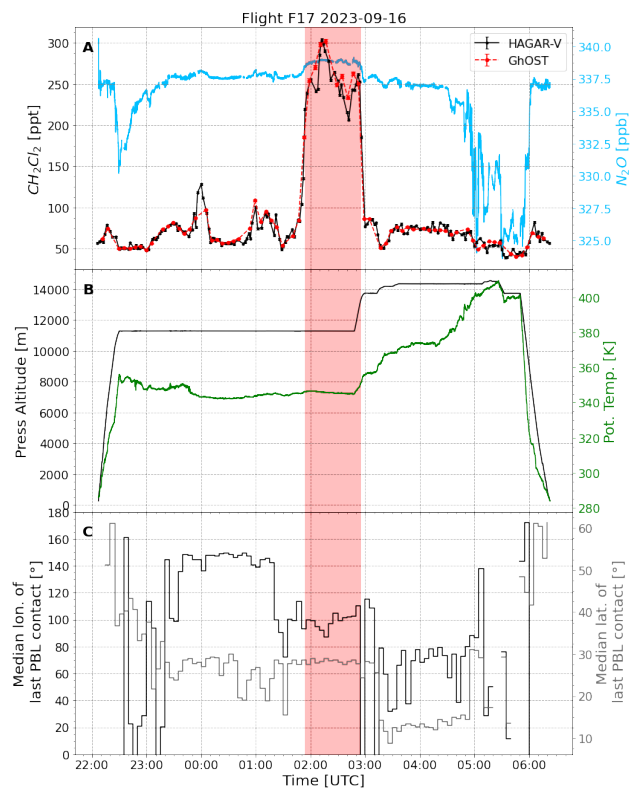
Figure 4. like Fig. 3 but for flight F17 on September 16, 2023.
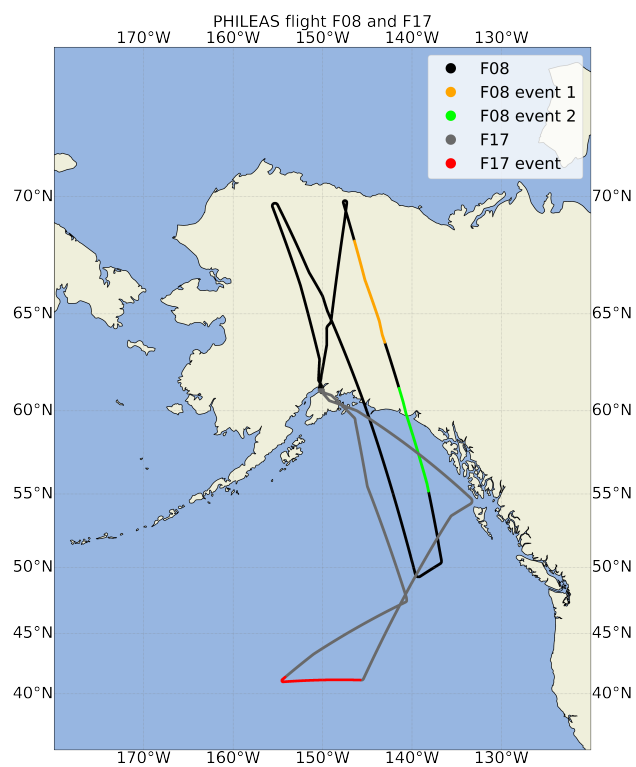
Figure 5. Flight tracks of flight F08 on August 26 (black) and flight F17 on September 16, 2023. Flight segments with high values of CH_2Cl_2 were highlighted in orange, green, and red (F08 event 1, F08 event 2, and F17 event, respectively).
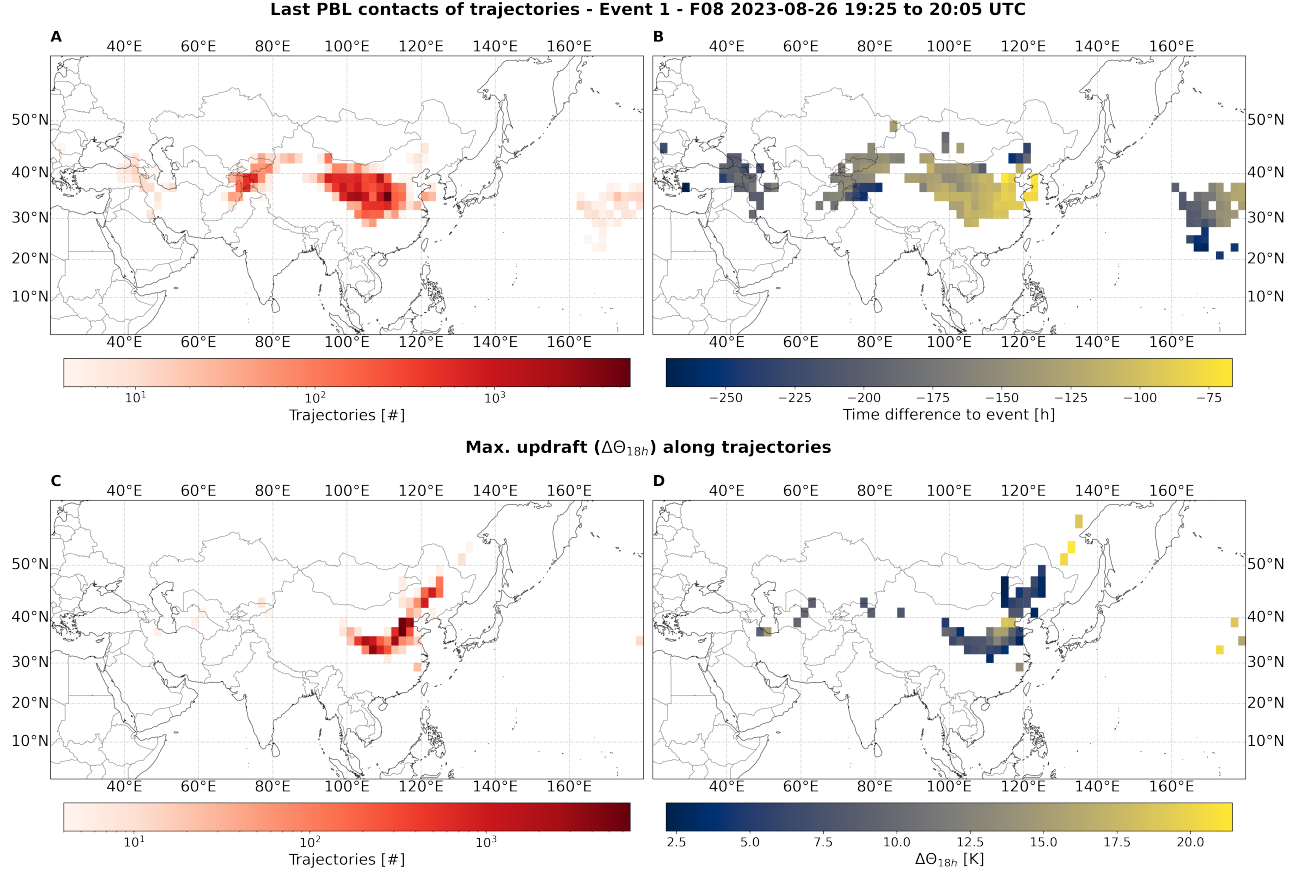
Figure 6. Averaged over $2.0°$ x $2.0°$ latitude-longitude intervals for the first event of flight F08, the last PBL contacts and maximum updrafts along the trajectories are shown. Panels **A** and **C** illustrate these intervals, color-coded by the logarithmic scale of trajectory densities for last PBL contacts and maximum updrafts. Panel **B** displays time differences to release time, using color-coded intervals in hours. Panel **D** displays the location of max. updraft within 18 h along the particle trajectories, color-coded by potential temperature difference within the 18 h
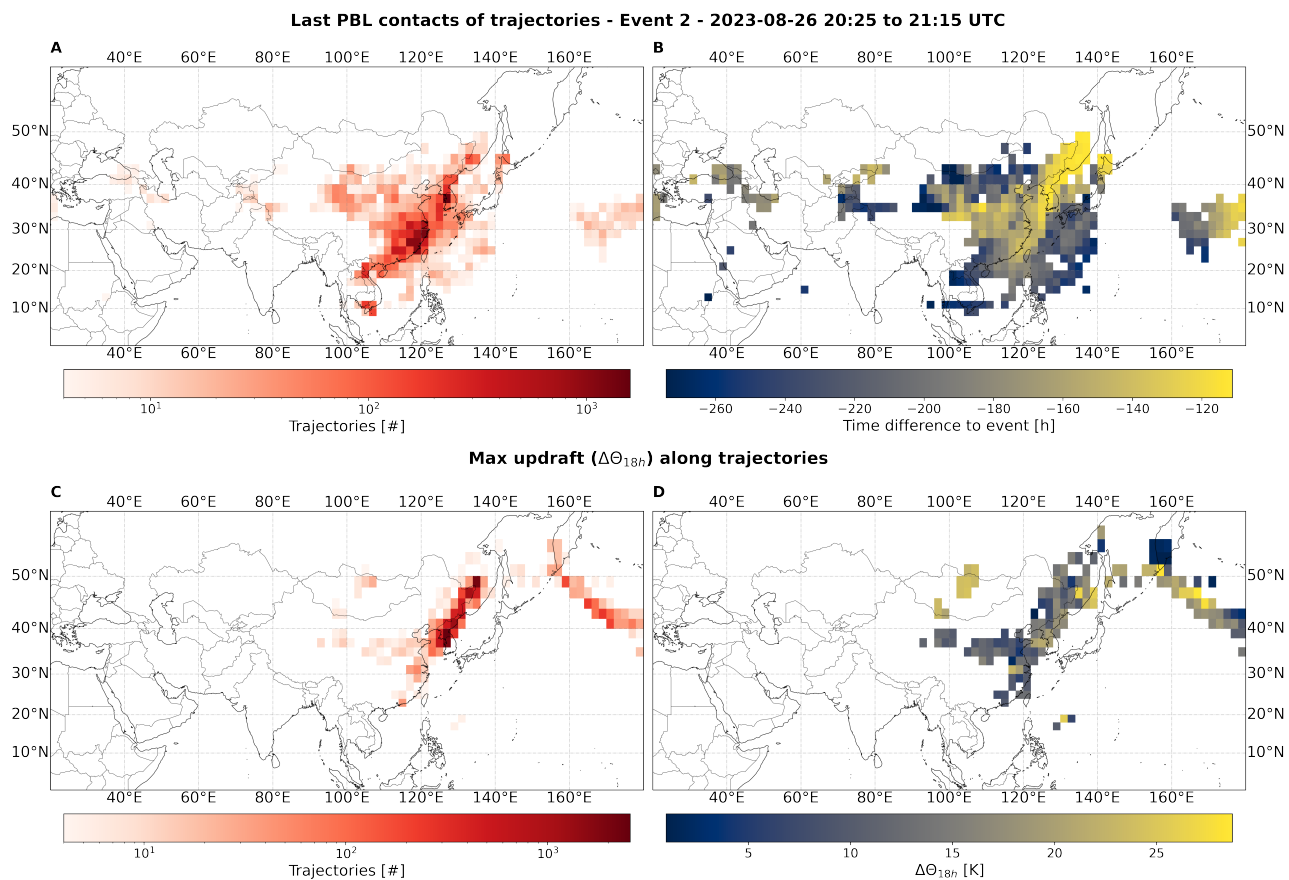
Figure 7. like Fig. 6, but for the second event on flight F08.
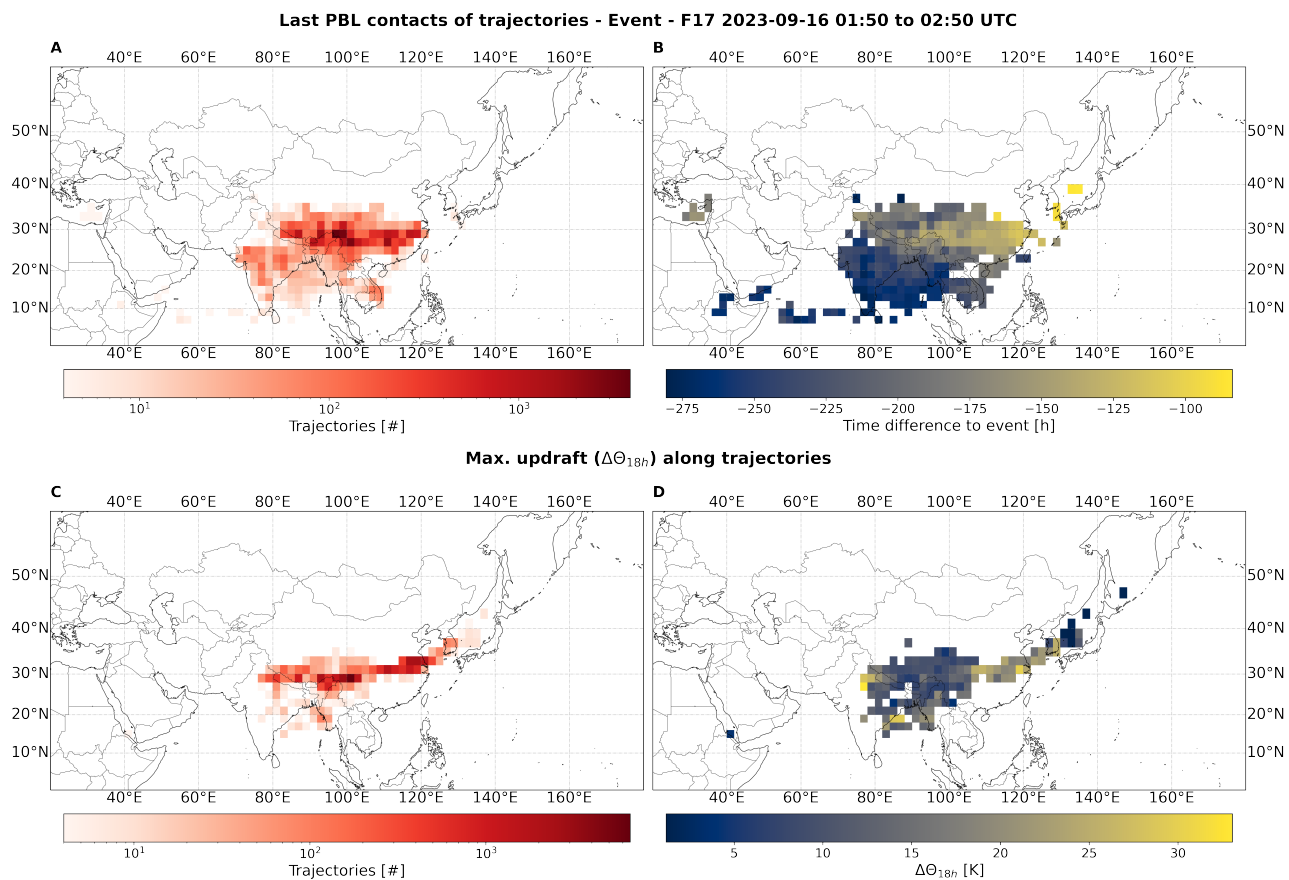
Figure 8. like Fig. 6, but for the event on flight F17.
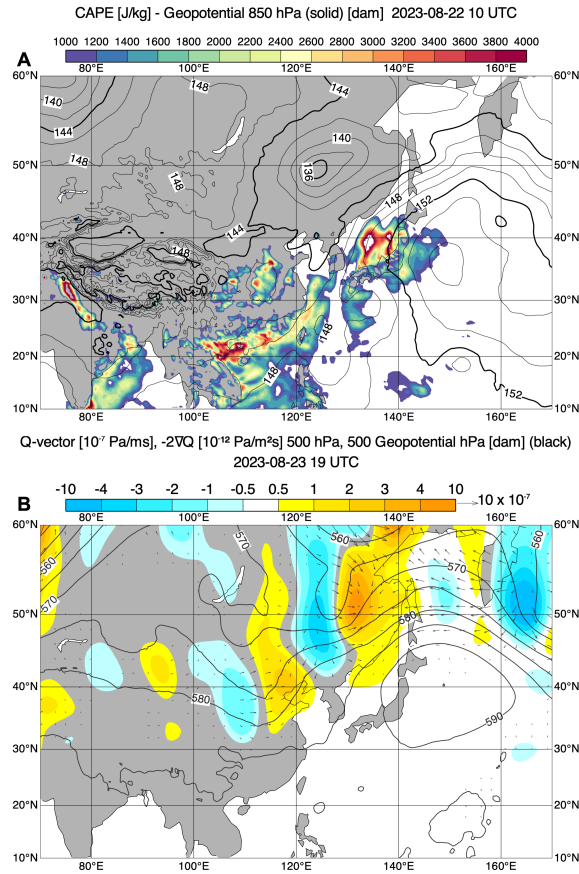
Figure 9. Analysis map from 2023-08-22 10 UTC (**A**) and 2023-08-23 19 UTC (**B**). **A** shows the vertical distribution of the Convective Available Potential Energy (CAPE) and 850 hPa geopotential. **B** shows Q-Vector, Q-Vector vergences, and 500 hPa geopotential.
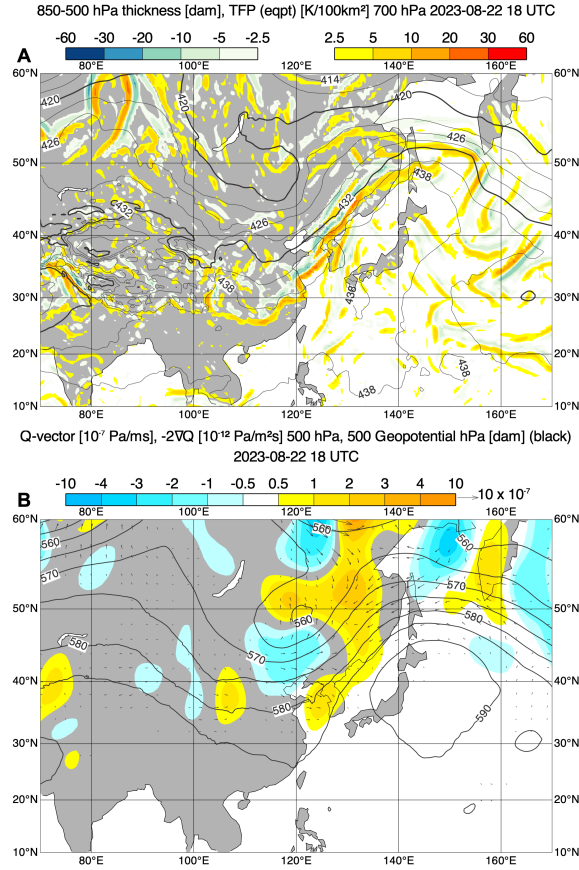
Figure 10. Analysis maps from 2023-08-22 18 UTC. **A** shows the thermal front parameter (TFP) and 850–500 hPa thickness. **B** shows Q-Vector, Q-Vector vergences, and 500 hPa geopotential.
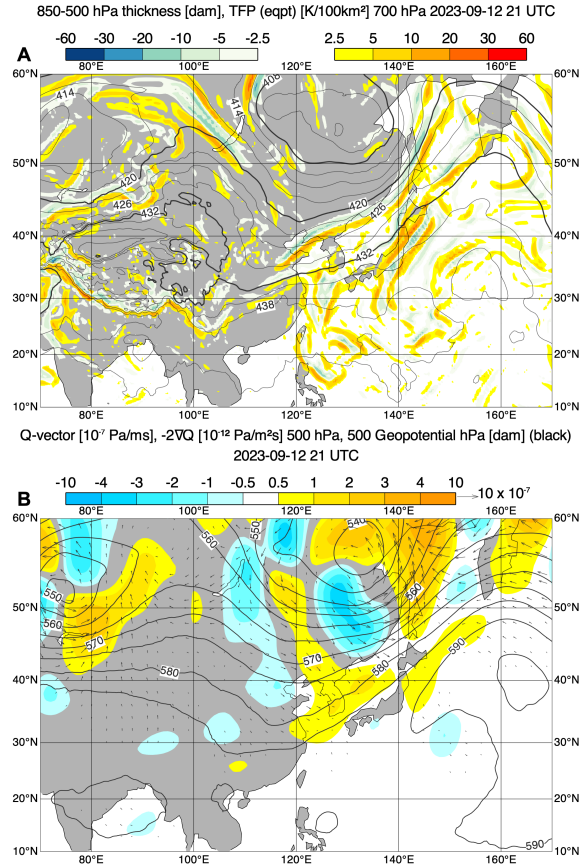
Figure 11. like Fig. 10, but for 2023-09-12 21 UTC.

Table 1. Percentage (%) of particle trajectories that are in a potential vorticity range of 2-4 PVU (tropopause region) or greater than 4 PVU (stratospheric). Given in 48 hour averages along the forward trajectories.

		Δ48h	Δ96h	Δ144h	Δ192h	Δ240h	Δ288h
F08 event 1	2-4 PVU	3.8	3.8	2.6	1.9	1.9	1.7
	>4 PVU	1.5	3.5	3.8	3.4	3.8	3.7
F08 event 2	2-4 PVU	0.0	0.1	6.3	8.9	3.3	2.6
	>4 PVU	0.0	0.0	0.3	1.0	1.5	2.4
F17 event	2-4 PVU	0.0	5.2	27.6	12.0	11.8	12.3
	>4 PVU	0.0	0.0	0.6	1.3	1.5	3.2